RSC
Applied Interfaces

PAPER

View Article Online
View Journal | View Issue

Cite this: *RSC Appl. Interfaces*, 2025, **2**, 1485

Phosphate conversion process on Al–Si-coated steel: characterization and impact on the heat-treatment performance†

Robin Dohr,*[ab] Dorothea Mattissen,[a] Michael Stang[a] and Uwe Ruschewitz *[b]

Received 21st March 2025,
Accepted 9th July 2025

DOI: 10.1039/d5lf00079c

rsc.li/RSCApplInter

Energy- and time-efficient hot-stamping processes are essential for the production of lightweight, high-performance automotive components. Aluminum–silicon (Al–Si)-coated steel, widely used in hot-stamping, suffers from low heating efficiency due to its reflective surface, limiting process speed and energy efficiency. In this study, a phosphate conversion process including alkaline cleaning and subsequent phosphate conversion was applied to aluminum–silicon (Al–Si-)-coated steel sheets to improve the heating rate during heat treatment. Surface characterization of the sheets was performed using field-emission scanning electron microscopy (FE-SEM), X-ray fluorescence (XRF), powder X-ray diffraction (PXRD), Fourier-transform infrared (FT-IR) spectroscopy with an integrating sphere, and X-ray photoelectron spectroscopy (XPS). Alkaline cleaning increased the surface concentration of silicon, which in turn decreased reflectance compared to untreated sheets, as confirmed by total reflectance measurements. Subsequent phosphate conversion formed a hopeite ($Zn_3(PO_4)_2 \cdot 4H_2O$) layer, further reducing the reflectance. *In situ* temperature curves, recorded using a thermocouple embedded in the sheets, revealed a significant reduction of the heating time for the cleaned and phosphated sheets. Longer phosphating durations progressively shortened the heating time by up to 50%, which correlated with an increase in surface emissivity of nearly 100%, thereby doubling the efficiency of the heating process. Characterization of the phosphated sheets after heat treatment revealed that the phosphate coating has reacted with aluminum from the Al–Si-layer to form $ZnAl_2O_4$ (gahnite) and $AlPO_4$ (tridymite-type). The dehydration of the hopeite layer was also studied under the heat-treatment conditions, which showed an amorphous, hydrated intermediate phase after 2 s at 920 °C and the formation of crystalline $Zn_3(PO_4)_2$ after 10 s.

Introduction

The demand for high-strength, lightweight automotive components has increased significantly, as manufacturers aim to reduce vehicle weight while improving crash performance. Al–Si-coated steel, specifically 22MnB5 steel, is commonly used in hot-stamping processes to produce high-strength parts with complex geometries. However, the production of these parts is both time- and energy-intensive, primarily due to high processing temperatures (~920 °C) and typical heating durations of 300 s.[1–4] The heating phase in hot-stamping, especially for Al–Si-coated steel, has been well-studied in terms of coating stability and behavior. During hot-stamping, the blanks are heated to 850–950 °C, followed by quenching and forming into high-strength components. At the high temperatures present in the furnace, heat transfer is governed by thermal radiation in the infrared range of the spectrum. The Al–Si coating, though effective in preventing oxidation, limits energy absorption due to its low emissivity in the infrared range.[5]

Phosphating of zinc-coated and uncoated steel as well as aluminum alloys is a commonly used surface conversion technique to enhance corrosion resistance and paint adhesion, making phosphate coatings an interesting option for enhancing the energy absorption during heat treatment.[6,7] Previous research has shown that phosphating of aluminum alloys and also Al–Si-coated steel results in the formation of a hopeite layer similar to phosphated zinc-coated steel.[7,8] However, in contrast to phosphating of zinc-coated steel, a fluoride additive in the phosphating bath is needed to dissolve the aluminum and form a hopeite layer. In the case of Al–Si coated steel, NH_4HF_2 has been shown to be an effective additive.[8]

In phosphate coatings, typically tricationic hopeite is formed, in which zinc is partially substituted by nickel and

---

[a] *thyssenkrupp Steel Europe AG, Kaiser-Wilhelm-Straße 100, 47166 Duisburg, Germany. E-mail: robin.dohr@thyssenkrupp-steel.com*

[b] *Department of Chemistry and Biochemistry, University of Cologne, Greinstraße 6, 50939 Köln, Germany. E-mail: uwe.ruschewitz@uni-koeln.de*

† Electronic supplementary information (ESI) available: XPS spectra, FE-SEM images, correlation between emissivity and heating time, and coding for phases identified in the PXRD patterns. See DOI: https://doi.org/10.1039/d5lf00079c

manganese ions within the crystal structure. The incorporation of Ni and Mn in the coating improves corrosion resistance and increases thermal stability.[9–11]

Previous work has suggested that phosphating can improve the heating efficiency of Al–Si-coated steel.[12,13] However, a detailed investigation into the process and phase transformations during heat treatment remains unexplored. This study investigates the effect of phosphating on the heating rate of Al–Si-coated steel, focusing on characterizing the phosphate coating before, during, and after heat treatment to understand its stability, transformations, and potential impact on process efficiency. In particular, this study addresses the possible phase transformations within the phosphate coating and the interactions between the coating and the Al–Si surface under heat treatment conditions, which have not been previously explored. Therefore, the total reflectance of the untreated reference and of the cleaned and phosphated surfaces prior to heat treatment was measured and compared to temperature curves recorded *in situ* in the furnace. Furthermore, the cleaned and phosphated surfaces were characterized in terms of chemical and phase composition using field-emission scanning electron microscopy (FE-SEM), X-ray fluorescence (XRF), powder X-ray diffraction (PXRD), Fourier-transform infrared (FT-IR) spectroscopy with an integrating sphere, and X-ray photoelectron spectroscopy (XPS).

Methods

Materials and preparation

Aluminum–silicon (Al–Si) hot-dip-coated steel sheets with a thickness of 1.5 mm (MBW® 1500+AS150) were provided by thyssenkrupp Steel Europe AG. The base material, MBW®1500, is a manganese–boron alloyed steel containing approximately 0.24 wt% C, 1.3 wt% Mn and 0.005 wt% B. The steel exhibits a ferritic–pearlitic microstructure in the as-received condition. The Al–Si hot-dip coating (AS150) has a thickness of ∼25 μm per side and consists of approximately 90 wt% Al, 10 wt% Si, and up to 4 wt% Fe. Sheets with a size of 100 mm × 200 mm were sectioned for further processing.

Cleaning and phosphating procedure

The alkaline cleaning and phosphating followed established protocols.[14] For cleaning, the sheets were immersed in 0.2 M NaOH at 60 °C for 10 s and subsequently rinsed with demineralized water. For the phosphated sheets, the cleaning was followed by immersion in an activation bath (Chemetall Gardolene® V6559, 3.9 mL per liter of demineralized water) for 60 s at room temperature. After activation, the sheets were phosphated in a tricationic phosphating solution containing zinc, nickel and manganese and phosphoric acid (Chemetall Gardobond® 26T) at 60 °C for varying phosphating times of 15 s, 30 s, 60 s, 90 s, and 120 s. NH_4HF_2 (95%, Alfa Aesar, 1.88 g per liter of phosphating solution) was used as a fluorine additive to aid aluminum dissolution and hopeite formation.

Heat treatment

Heat treatment and temperature monitoring were carried out in a Nabertherm N41/H furnace with a thermocouple type k (0.5 mm, NiCr/NiAl) at 920 °C for 300 s. The thermocouple was embedded in the sheets through a drilled hole (0.5 mm in diameter and 6 mm deep) located on the side of the sheets. Subsequent quenching for 15 s at 3 MPa was realized by using water cooled hydraulic plates. Although the furnace was set to a target temperature of 920 °C, the time required to reach 900 °C (t_{900}) was used for comparison of the heating efficiency. By using t_{900}, a reliable comparison of the heating time was achieved, unaffected by temperature fluctuations near the target temperature.

Total reflectance spectra were recorded between 600 cm^{-1} and 10 000 cm^{-1} with a gold-plated integrating sphere (Bruker Optik, type A 562-G) and an MCT detector coupled to a Bruker Vertex 70 FT-IR spectrometer. The spectra were combined (KBr beam-splitter: 600–6500 cm^{-1}, quartz beam-splitter: 3500–10 000 cm^{-1}) in Bruker Opus software (version 8.8, Bruker Optik GmbH, Ettlingen, Germany). The emissivity (ε_{920}) was calculated from the total reflectance spectra (ρ_λ) and the blackbody radiation at 920 °C (i_λ) in the range of 600 cm^{-1} to 10 000 cm^{-1} using eqn (1) given below.

$$\varepsilon_T = 1 - \int_{\lambda 1}^{\lambda_2} \rho_\lambda \cdot i_\lambda(T) \mathrm{d}\lambda \Big/ \int_{\lambda 1}^{\lambda_2} i_\lambda(T) \mathrm{d}\lambda \tag{1}$$

The blackbody spectrum $i_\lambda(T)$ is given by eqn (2).[15]

$$i_\lambda(T) = \frac{2\pi hc^2}{\lambda^5} \frac{1}{e^{hc/\lambda k_B T} - 1} \tag{2}$$

Surface and phase characterization

PXRD analysis of the sheets was performed on a Philips X'Pert MPD Pro with a Co source (Co$K_{\alpha 1}$ = 1.78901 Å, Co$K_{\alpha 2}$ = 1.79290 Å, with a ratio $K_{\alpha 2} : K_{\alpha 1}$ = 0.5) and a Xe-filled proportional detector, using a grazing-incidence angle of 2° over 5–65° (2θ). Data were collected with a step size of 0.025° (2θ) and a time per step of 1 s. For an improved analysis of the phosphated sheet after heat treatment, the surface was removed by scratching with a stainless-steel knife. A PXRD scan of the powder was recorded using a Stoe StadiP (Debye–Scherrer geometry) equipped with a Ge(111)-monochromator and a "DECTRIS MYTHEN" detector (Mo$K_{\alpha 1}$ = 0.70930 Å) over 0–60° (2θ). Data were collected with a step size of 0.015° (2θ) and a time per step of 1620 s.

The surface morphology of the prepared sheets was studied using a field-emission scanning electron microscope (FE-SEM, Zeiss LEO 1530) and an energy dispersive X-ray system (EDS, Oxford X-Max 80).

The phosphorus content was determined using a handheld X-ray fluorescence system (XRF, Bruker S1 Titan

800) at 10 kV and 50 μA, with the reported value representing the average of three measurements per sample. X-ray photoelectron spectroscopy (XPS) was used to determine the elemental surface composition and binding energies of both the reference and cleaned sheets. Measurements were carried out on a Phi Quantera II SXM (Physical Electronics) equipped with a monochromatic Al X-ray source ($h\nu$ = 1486.6 eV) at a base pressure of 2×10^{-9} mbar. All spectra were referenced to the adventitious carbon signal (284.6 eV). Data processing, fitting and quantification were done in the CasaXPS software.[16]

Results and discussion

To investigate the impact of alkaline cleaning on the Al–Si-surface, the sheets before and after cleaning were characterized using FE-SEM and XPS. The FE-SEM micrographs in Fig. 1 illustrate the surface morphology and elemental contrast of Al–Si-coated steel sheets before and after alkaline cleaning. The SE-image of the reference surface is homogeneous with low contrast, indicating a uniform alumina layer on the surface. However, the BSE-image shows a variation of the material contrast due to underlying features. The EDS analysis of the cleaned surface shows the presence of an Al-matrix as well as Si-rich and Al–Fe–Si phases. In contrast to the reference surface, the SE-image of the cleaned sheet exhibits a distinct morphology characterized by etching grooves along the edges of silicon-rich regions.

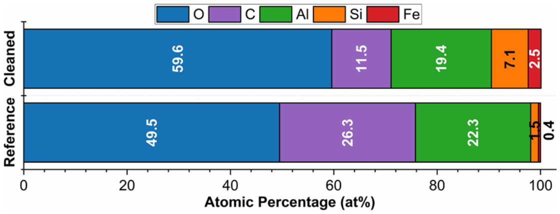

Fig. 2 Elemental composition from the XPS measurements for the reference and cleaned Al-Si-coated steel sheets.

Fig. 2 shows the surface elemental compositions of the reference and cleaned samples derived from XPS measurements. Compared to the reference sheet, the cleaned sheet shows an increased relative surface concentration of Si and Fe, alongside a reduction in C and Al. The high-resolution XPS spectra of the Al 2p and Si 2p transitions reveal aluminum oxide as well as elemental aluminum and silicon on the reference sheet, and additionally silicon oxide on the cleaned sheet (Fig. S1†). This suggests the dissolution of the alumina layer on the reference sheet during the cleaning process, followed by the formation of oxides on both Al- and Si-rich areas caused by the cleaning process and an oxidizing atmosphere. Additionally, the evolution of H_2 gas during the cleaning process indicated the oxidation and dissolution of surface aluminum. The exposure of the Si-rich and Al–Fe–Si phases and the formation of etching grooves suggest a non-uniform dissolution behavior of the Al–Si coating in the alkaline medium, with the aluminum matrix, as expected, being more susceptible to oxidation and dissolution.

In the subsequent phosphating step, plate-like hopeite crystals form primarily on top of the Si-rich phases after just 15 s of phosphating (Fig. 3). EDS analysis shows that these crystals consist of Zn, P, O, Mn and Ni. The analysis also contains Si and Al from the Al–Si-coating. With increasing

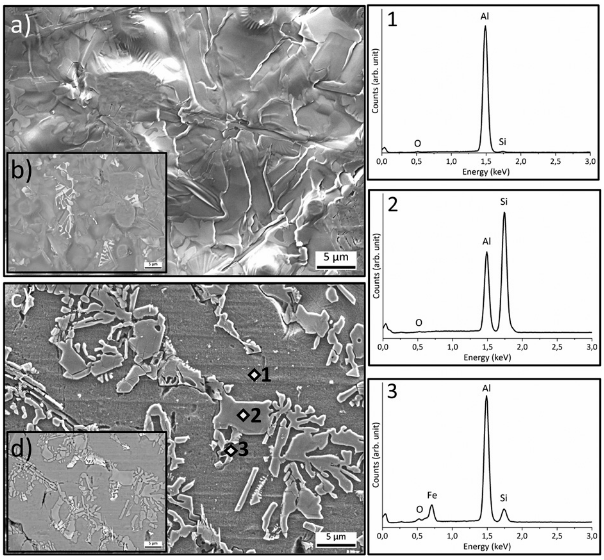

Fig. 1 FE-SEM micrographs showing the surface morphology (a and c: secondary electron (SE) images) and elemental contrast (b and d: backscattered electron (BSE) images) before (a and b) and after cleaning (c and d). Right panel: EDS spectra taken on the cleaned sample at different spots (marked with "◊" in c) giving the elemental composition of the different phases observed (1: Al-rich, 2: Si-rich, and 3: Al–Fe–Si phases).

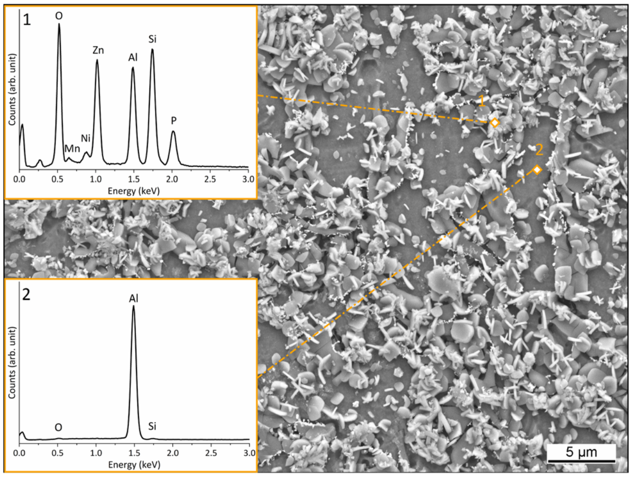

Fig. 3 FE-SEM image of the Al–Si-coated steel surface after 15 s of phosphating, showing the formation of hopeite crystals. The two EDS spectra correspond to distinct regions of the surface: the upper spectrum (1) represents a crystal-covered area, confirming the presence of Zn, Mn, Ni, P, and O typical for hopeite, while the lower spectrum (2) represents a bare region of the Al–Si coating, predominantly showing Al.

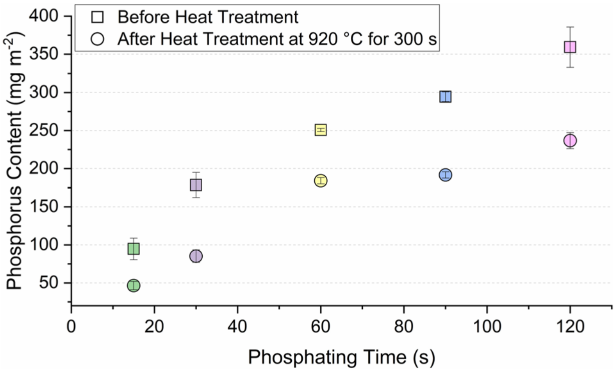

Fig. 4 Phosphorus content on the sheet surface before and after heat treatment (920 °C for 300 s) as a function of phosphating time.

phosphating time, the crystals gradually cover more of the Al–Si surface, forming a continuous layer after 120 s of phosphating (Fig. S2†). The phosphorus content, measured *via* X-ray fluorescence, increases with phosphating time, reaching a maximum of 359 mg m^{-2} after 120 s (Fig. 4). The increase in the phosphorus content follows a saturation-like trend, although complete saturation is not reached within the maximum phosphating time applied here. The phosphorus content on the surface after heat treatment was significantly lower (approximately 60% reduction) compared to the level before heat treatment.

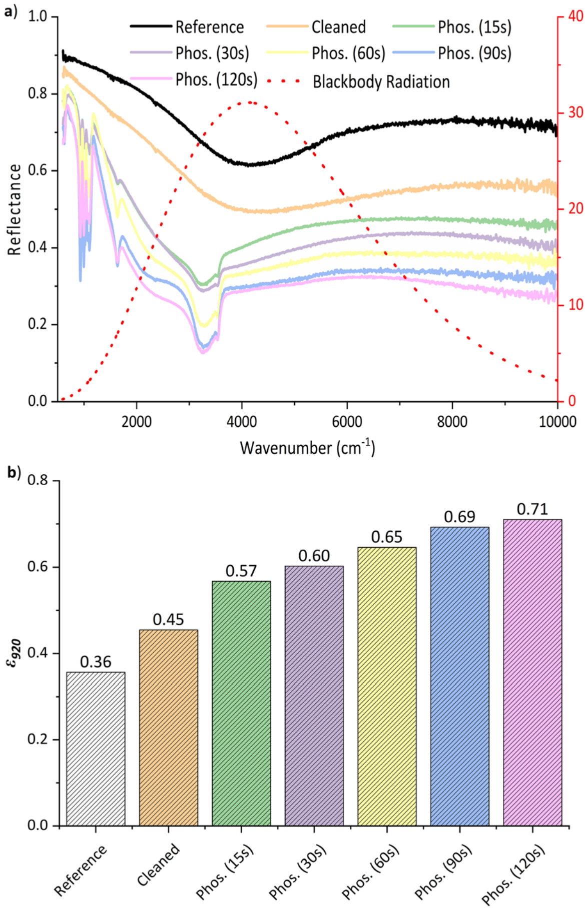

Fig. 5 Total reflectance spectra of the surfaces (a) and corresponding emissivity values (ε_{920}) calculated from the reflectance data using the blackbody radiation spectrum (b).

Next, the total reflectance spectra and corresponding emissivity (ε_{920}) of the as-prepared sheets were measured (Fig. 5). The reference sheet showed the highest reflectance in the far-infrared range, with a minimum at approximately 4000 cm^{-1}, close to the blackbody radiation maximum (~4120 cm^{-1}). The reflectance of the cleaned sheet was significantly lower across the entire spectral range, and the phosphated sheets exhibited even further reductions in reflectance as the phosphating time increased. The decrease in reflectance corresponded to emissivity values increasing from 0.36 (reference) to 0.47 (cleaned) and further to 0.71 (120 s phosphated), thus nearly doubling the emissivity compared to the untreated surface. Additionally, strong vibrational bands of hopeite were observed in the spectra (Fig. 5, Table 1).[17] Aside from these vibrational bands, the minimum reflectance values of the processed sheets occurred close to the spectral range observed for the reference sheet (~4000 cm^{-1}).

Based on the significantly increased emissivity values, higher heating rates and reduced heating times to 900 °C (t_{900}) were anticipated for the processed sheets. *In situ* temperature measurements using a thermocouple embedded in the sheets confirmed these expectations (Fig. 6). In comparison with the reference sheet, the cleaned and, very distinctively, the phosphated sheets exhibit significantly reduced heating times to reach 900 °C (t_{900}). The fastest sheet (120 s phosphated) reaches the target temperature nearly twice as fast as the reference, effectively doubling the heating process efficiency. These reduced heating times directly correlate with the emissivity values previously discussed. The

Table 1 Assignment of IR-active modes observed in the FT-IR spectra of the phosphated sheets before and after heat treatment (Fig. 9)

Observed frequencies (cm^{-1})	Assignment	References
Phosphated, before heat treatment		
1120–940	ν_3 mode of tetrahedral $[PO_4]^{3-}$	17
970–920	ν_1 mode of tetrahedral $[PO_4]^{3-}$	
640	ν_4 mode of tetrahedral $[PO_4]^{3-}$	
3600–3000	O–H stretching	
1650–1600	H–O–H bending	
3545	Free hydroxyl stretching	
Phosphated, heat-treated at 920 °C, 2 s		
~1070	Low-resolved band of tetrahedral $[PO_4]^{3-}$	17
3400–3200	O–H stretching	
1650–1600	H–O–H bending	
Phosphated, heat-treated at 920 °C, 10 s		
~1050	Low-resolved band of tetrahedral $[PO_4]^{3-}$	17
Phosphated, heat-treated at 920 °C, 300 s		
1113	$[PO_4]^{3-}$ unit in tridymite $AlPO_4$	33, 34

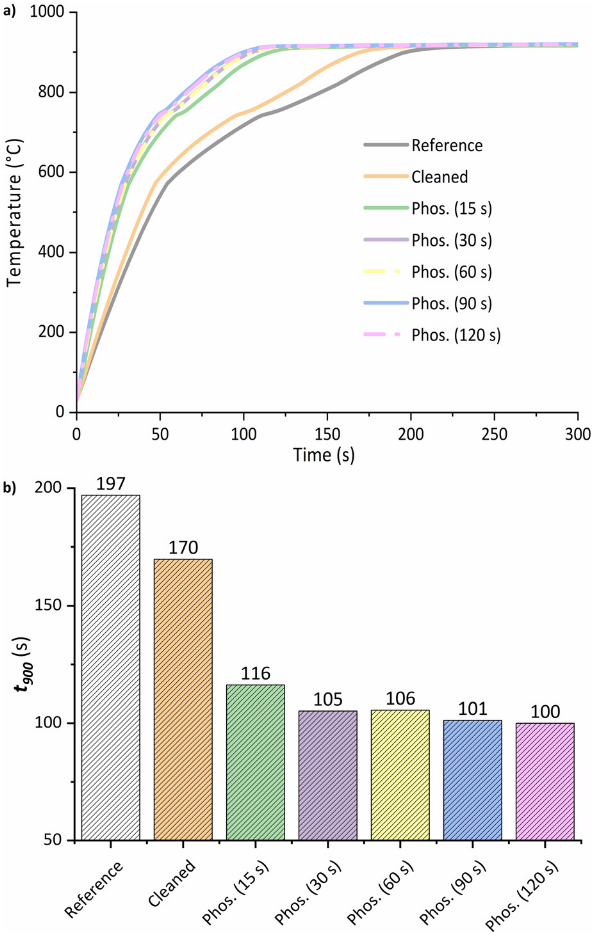

Fig. 6 Temperature curves (a) and time required to reach 900 °C (t_{900}) (b) for the reference, cleaned, and phosphated surfaces.

temperature curves followed a saturation trend, as the sheets approached the furnace temperature of 920 °C. At two specific temperatures, the temperature curves of all sheets show sudden drops in the heating rate. The first, at 574 °C, closely coincides with the eutectic melting temperature of the Al–Si coating (577 °C).[18–20] This melting of the Al–Si coating is known to cause a temporary drop in emissivity, thereby slowing down the heating rate.[21,22] The second decline, at 742 °C, is attributed to the ferrite to austenite phase transition in the steel, which is known to be an endothermic process.[20] The fact that the decrease of the heating rate at 574 °C was observed in the reference sheet as well as in the processed sheets indicates that surface melting still occurs and affects the absorption of the furnace radiation on the processed sheets.

While the phosphate coating itself contributes to absorption through its vibrational bands, a significant portion of absorption also occurs at the underlying Al–Si phases.

The FE-SEM images of the reference, alkaline-cleaned, and phosphated sheets (120 s) before and after heat treatment (920 °C, 300 s) reveal substantial changes in the surface morphology (Fig. 7). The reference sheet transitions from a smooth surface to a roughened surface due to melting and diffusion of iron into the Al–Si-coating.[23] The cleaned sheet also shows increased roughness after the heat treatment. The needle-shaped Si-rich phases exposed by the alkaline cleaning remain visible after the heat treatment, indicating that they did not contribute to alloy formation as observed in the reference sheet. This could result from physical separation of the topmost Si-rich phases from the reacting matrix and/or oxidation of Si after the cleaning process, which was evident in the XPS data (Fig. 2 and S1†). The phosphated surface before heat treatment shows a uniform, crystalline hopeite layer. After the heat treatment, the surface becomes rough and inhomogeneous with crater-like areas and spots, which show a micro- to nanocrystalline structure.

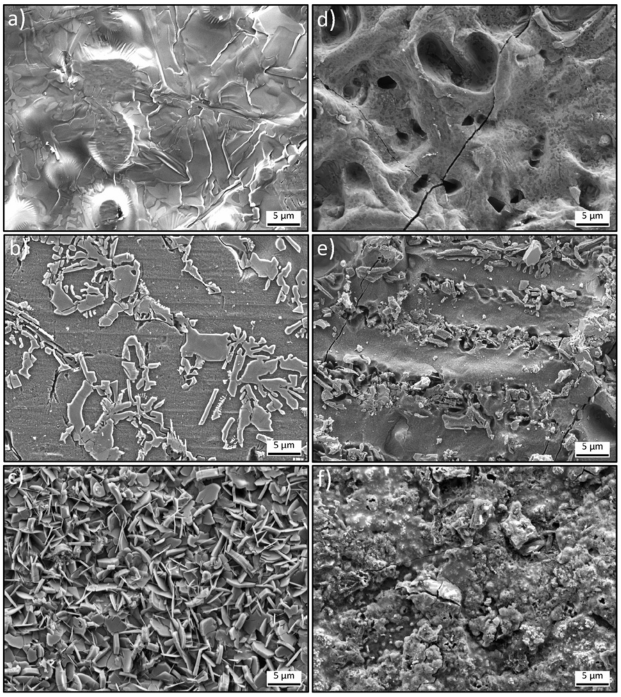

Fig. 7 FE-SEM images before (a–c) and after (d–f) heat treatment at 920 °C for 300 s of the reference sheet (a and d), alkaline cleaned sheet (b and e) and phosphated (120 s) sheet (c and f).

To further investigate these changes on the phosphated sheet, PXRD scans and IR spectra were collected for the sheet with a phosphating time of 120 s before and after heat treatment durations of 2, 10, and 300 s. Heat-treatment durations of 2 and 10 s were chosen to investigate the dehydration of hopeite under the process conditions. The PXRD pattern of the phosphated surface after 120 s confirms the presence of hopeite ($Zn_3(PO_4)_2{\cdot}4H_2O$), as well as silicon and aluminum from the Al–Si coating (Fig. 8). Although the formation of hopeite on an Al–Si coating has been investigated previously, no continuous layer has been reported until now.[8] The PXRD pattern after 2 s of heating at 920 °C indicated a non-crystalline dehydration product of hopeite. After 10 s of heating, crystalline zinc phosphate anhydrate ($Zn_3(PO_4)_2$) was formed. After 300 s, the diffraction pattern revealed the presence of Al_5Fe_2 as the primary phase, formed due to iron diffusion from the steel,

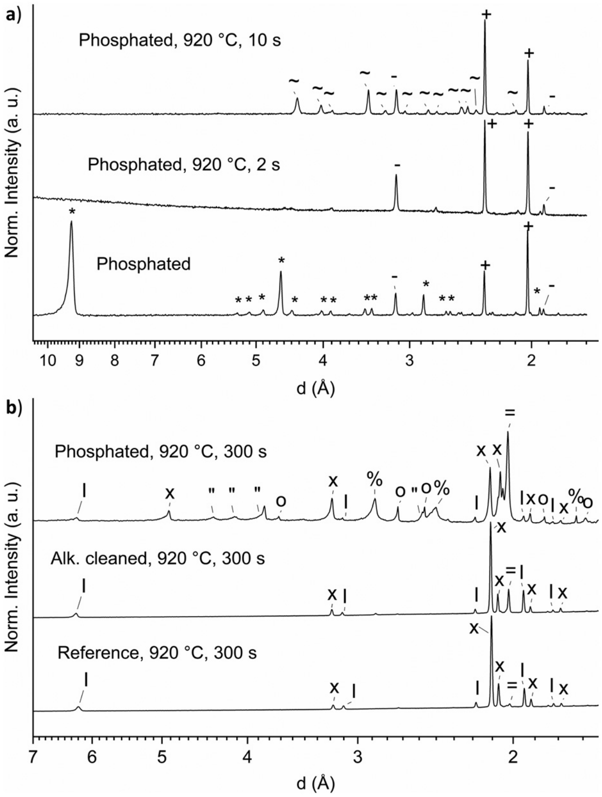

Fig. 8 (a) PXRD patterns of the phosphated sheet (120 s) before heat treatment and after heat treatment at 920 °C for 2 s and 10 s. (b) PXRD patterns of the reference, alkaline-cleaned, and phosphated sheets (120 s) after 300 s of heat treatment at 920 °C. Phase assignment: $Zn_3(PO_4)_2\cdot4H_2O$ (*),[25] Si (–),[26] Al (+),[27] $Zn_3(PO_4)_2$ (~),[25] Fe_2Al_5 (x),[28] $AlPO_4$ (tridymite-type) (″),[29,30] Fe_2O_3 (o),[41] $ZnAl_2O_4$ (%),[32] and Fe (=).[31] Unidentified reflections most likely belong to Al–Fe–Si phase(s) (I). Detailed phase assignments are given in Table S1.†

alongside Fe (α-ferrite), $ZnAl_2O_4$ (gahnite), $AlPO_4$ (tridymite type structure), Fe_2O_3 (hematite) and additional unidentified reflections (Fig. 8). Crystalline Al–Fe–Si phases with varying stoichiometries are commonly observed in Al–Si-coatings after heat-treatment.[35–40] The unidentified reflections observed here are visible in the diffraction patterns of the reference, alkaline cleaned, and phosphated sheets. Therefore, we assume that they most likely belong to one or multiple Al–Fe–Si phase(s).

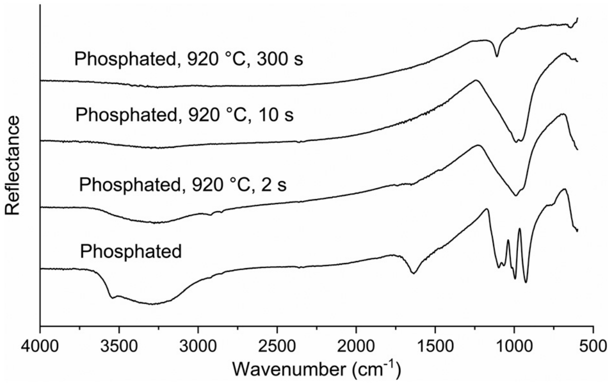

Fig. 9 FT-IR spectra of the phosphated sheet (120 s) before and after heat treatment (2, 10, and 300 s at 920 °C). Assignments of the IR-active modes are provided in Table 1.

The IR spectra of the phosphated sheet (120 s), presented in Fig. 9, show distinct phase transformations, as the sample undergoes heat treatment at 920 °C for varying durations (2, 10, and 300 s). Initially, the spectrum of the untreated phosphated surface exhibits characteristic vibrational modes of hopeite, with strong bands associated with the tetrahedral $[PO_4]^{3-}$ unit at 1120–940 cm^{-1}, 970–920 cm^{-1}, and 640 cm^{-1}, along with O–H stretching and bending modes (3600–3000 cm^{-1}, 1650–1600 cm^{-1}) from structurally bound water (Table 1). After 2 s of heat treatment, the sharp band at 3454 cm^{-1} disappears and the overall intensity of the IR bands corresponding to water is reduced, indicating partial dehydration of hopeite. A broad, low-resolved $[PO_4]^{3-}$ band at around 1070 cm^{-1} emerges, indicating the transition to a less hydrated form of hopeite. This is consistent with the formation of an X-ray amorphous phase, as observed in the PXRD scans (Fig. 8a). This initial dehydration step is consistent with the findings of Paluszkiewicz *et al.*, who observed similar changes of IR-active bands for the dihydrate of zinc phosphate ($Zn_3(PO_4)_2\cdot2H_2O$), attributing them to structural changes within the crystal structure.[17] Upon further heating for 10 s, the water-related bands vanish and the spectrum shows a shift of the main phosphate band to approximately 1050 cm^{-1}, consistent with the formation of anhydrous zinc phosphate ($Zn_3(PO_4)_2$) as observed in the PXRD scans (Fig. 8). Finally, after 300 s at 920 °C, the IR spectrum is dominated by a peak at 1113 cm^{-1}, most likely corresponding to the $[PO_4]^{3-}$ unit in tridymite-type $AlPO_4$.[33,34]

During heating, the Al–Si coating melts, resulting in a highly reactive, Al-rich surface. The anhydrous zinc phosphate very likely reacts with this Al-rich surface to form $ZnAl_2O_4$ and $AlPO_4$ as corroborated by PXRD and IR-spectroscopy. The reaction probably leads to the release of P_4O_{10} from the surface, which explains the observed reduction in the phosphorus content observed *via* XRF after heat treatment (Fig. 4). Similar decomposition of hopeite to ZnO was observed previously on phosphated, zinc-coated steel, after the surface was plasma-treated.[24]

Conclusions

The results of our work demonstrate that surface modification, particularly phosphating, significantly increases the emissivity and consequently enhances the heating rate of Al–Si-coated steel sheets during hot stamping. The phosphating results in a hopeite layer which undergoes distinct chemical transformations during heat treatment. Initially, hopeite dehydrates into amorphous, partially hydrated zinc phosphate, which, under continuous heating, subsequently crystallizes into anhydrous zinc phosphate ($Zn_3(PO_4)_2$). At high temperatures, $Zn_3(PO_4)_2$ reacts with the Al–Si coating and decomposes into $ZnAl_2O_4$ and $AlPO_4$, accompanied by the release of volatile phosphorous species like P_4O_{10}. Despite these reactions, the phosphate coating remains beneficial for heat absorption. Phosphated sheets require noticeably shorter heating times compared to the untreated reference sheets, indicating that phosphating can be an effective strategy for improving the processing speed and energy consumption in industrial hot-stamping processes.

Data availability

The data that support the findings of this study are available in the ESI† of this article. Additional information may be obtained from the authors upon reasonable request.

Author contributions

R. D.: investigation, formal analysis, writing – original draft; M. S.: resources, writing – review & editing; D. M.: resources, writing – review & editing; U. R.: supervision, resources, writing – review & editing.

Conflicts of interest

There are no conflicts to declare.

Acknowledgements

The authors would like to thank Gregor Müller, Fabian Junge, Maria Köyer, and Christian Altgassen for their valuable discussions and support. We also thank Kay Kämmerer for conducting the FE-SEM analysis, Stefanie Wierhake for the XPS investigations, and Manfred Völker for performing the PXRD measurements.

Notes and references

1 H. Karbasian and A. E. Tekkaya, *J. Mater. Process. Technol.*, 2010, **210**, 2103.
2 F. Ozturk, I. Kacar and M. Koç, in *Modern Manufacturing Processes*, ed. M. Koç and T. Özel, Wiley, 2019, pp. 239–264.
3 Z. Hou, Y. Liu, Q. He, J. Wang and J. Min, *Automot. Innov.*, 2023, **6**, 324.
4 Z. Wang, Q. Lu, Z. H. Cao, H. Chen, M. X. Huang and J. F. Wang, *Acta Metall. Sin.*, 2023, **36**, 1123.
5 C. Shi, K. J. Daun and M. A. Wells, *Metall. Mater. Trans. B*, 2016, **47**, 3301.
6 W. Rausch, *The Phosphating of Metals*, Finishing Publications, 1990.
7 W. H. Kok, X. Sun, L. Shi, K. C. Wong, K. A. R. Mitchell and T. Foster, *J. Mater. Sci.*, 2001, **36**, 3941.
8 P. Schneider, R. Sigel, M. M. Lange, F. Beier, F. U. Renner and A. Erbe, *ACS Appl. Mater. Interfaces*, 2013, **5**, 4224.
9 A. Arnaud, *Surf. Coat. Technol.*, 1988, **34**, 315.
10 B. Herbáth, K. Kovács, M. Jakab and É. Makó, *Crystals*, 2023, **13**, 369.
11 O. Girčienė, R. Ramanauskas, L. Gudavičiūtė and A. Martušienė, *Chemija*, 2013, **24**, 182.
12 R. Dohr, M. Köyer and F. Junge, WO2024/200152A1, 2024.
13 C. Altgassen, R. Dohr, M. Köyer and M. Stang, DE102023114525A1, 2023.
14 A. Erbe, P. Schneider, C. Gadiyar and F. U. Renner, *Electrochim. Acta*, 2015, **182**, 1132.
15 M. Planck, *Ann. Phys.*, 1901, **4**, 553.
16 N. Fairley, V. Fernandez, M. Richard-Plouet, C. Guillot-Deudon, J. Walton, E. Smith, D. Flahaut, M. Greiner, M. Biesinger, S. Tougaard, D. Morgan and J. Baltrusaitis, *Appl. Surf. Sci. Adv.*, 2021, **5**, 100112.
17 C. Paluszkiewicz, A. Stoch, A. Brożek and E. Długoń, *J. Mol. Struct.*, 1993, **293**, 291.
18 L. Cho, L. Golem, E. J. Seo, D. Bhattacharya, J. G. Speer and K. O. Findley, *J. Alloys Compd.*, 2020, **846**, 156349.
19 J. L. Murray and A. J. McAlister, *Bull. Alloy Phase Diagrams*, 1984, **5**, 74.
20 S. J. Grauer, E. Caron, N. L. Chester, M. A. Wells and K. J. Daun, *J. Mater. Process. Technol.*, 2015, **216**, 89.
21 C. M. Klassen and K. J. Daun, *Surf. Coat. Technol.*, 2020, **393**, 125795.
22 C. M. Klassen, R. D. L. Smith and K. J. Daun, *Mater. Charact.*, 2022, **189**, 112002.
23 M. Barreau, C. Méthivier, T. Sturel, C. Allely, P. Drillet, S. Cremel, R. Grigorieva, B. Nabi, R. Podor, J. Lautru, V. Humblot, J. Landoulsi and X. Carrier, *Mater. Charact.*, 2020, **163**, 110266.
24 J. Duchoslav, A. Himmelbauer, P. Kürnsteiner, H. Groiss, M. Kehrer, T. Stehrer and D. Stifter, *Appl. Surf. Sci.*, 2024, **665**, 160308.
25 M. C. Morris, H. F. McMurdie, E. H. Evans, B. Paretzkin and J. H. de Groot, *Standard X-Ray Diffraction Powder Patterns. Section 16: Data for 86 Substances*, National Bureau of Standards, U.S. Department of Commerce, 1979.
26 M. C. Morris, H. F. McMurdie, E. H. Evans and B. Paretzkin, *Standard X-Ray Diffraction Powder Patterns. Section 13: Data for 58 Substances*, National Bureau of Standards, U.S. Department of Commerce, 1976.
27 H. E. Swanson and E. Tatge, *Standard X-Ray Diffraction Powder Patterns*, National Bureau of Standards, U.S. Department of Commerce, 1953.
28 M. Ellner and J. Mayer, *Scr. Metall. Mater.*, 1992, **26**, 501.
29 O. W. Florke, *Z. Kristallogr.*, 1967, **125**, 134.
30 R. Debnath and J. Chaudhuri, *J. Solid State Chem.*, 1992, **97**, 163.
31 H. E. Swanson, N. T. Gilfrich and G. M. Ugrinic, *Standard X-Ray Diffraction Powder Patterns*, National Bureau of Standards, U.S. Department of Commerce, 1955.
32 H. Saalfeld, *Z. Kristallogr. Cryst. Mater.*, 1964, **120**, 476.
33 M. Rokita, M. Handke and W. Mozgawa, *J. Mol. Struct.*, 2000, **555**, 351.
34 S. Sri Rajeswary and C. Kannan, *Fuel*, 2025, **379**, 132946.
35 V. Kucera, M. Cabibbo, F. Průša, J. Fojt, J. Petr-Soini, T. Pilvousek, M. Kolaříková and D. Vojtěch, *Materials*, 2021, **14**, 1125.
36 P. P. Dey, P. Modak, A. Ghosh, D. Chakrabarti, P. S. Banerjee and M. Ghosh, *Results Mater.*, 2020, **6**, 100078.

37 M. Windmann, A. Röttger and W. Theisen, *Surf. Coat. Technol.*, 2014, **246**, 17.

38 J. Zhang, K. J. Daun and R. D. L. Smith, *ACS Omega*, 2023, **8**, 27002.

39 S. Wu, A. Bardelcik, C. Chiriac and C. Shi, *Coatings*, 2024, **14**, 399.

40 S. Wu, A. Bardelcik, C. Chiriac, A. Elsayed and C. Shi, *Surf. Coat. Technol.*, 2023, **471**, 129913.

41 M. C. Morris, H. F. McMurdie, E. H. Evans, B. Paretzkin, H. S. Parker and N. C. Panagiotopoulos, *Standard X-Ray Diffraction Powder Patterns. Section 18: Data for 58 Substances*, 1981.